Materials Science & Engineering C 127 (2021) 112196

Contents lists available at ScienceDirect

Materials Science & Engineering C

journal homepage: www.elsevier.com/locate/msec

Cellulose aerogel micro fibers for drug delivery applications

Matin Rostamitabar [a,b], Raman Subrahmanyam [c,d], Pavel Gurikov [c,d], Gunnar Seide [a], Stefan Jockenhoevel [a,b], Samaneh Ghazanfari [a,b,*]

[a] Aachen-Maastricht Institute for Biobased Materials (AMIBM), Faculty of Science and Engineering, Maastricht University, Urmonderbaan 22, 6167 RD Geleen, the Netherlands

[b] Department of Biohybrid & Medical Textiles (BioTex), AME-Helmholtz Institute for Biomedical Engineering, RWTH Aachen University, Forckenbeckstrabe 55, 52072 Aachen, Germany

[c] Laboratory for Development and Modelling of Novel Nanoporous Materials, Hamburg University of Technology, Eißendorfer Straße 38, 21073 Hamburg, Germany

[d] Aerogelex UG, Barlachstr. 2, 21073 Hamburg, Germany

ARTICLE INFO

Keywords:
Cellulose aerogel
Microfibers
Supercritical CO_2
Wet spinning
Drug delivery

ABSTRACT

Textile engineering can offer a multi-scale toolbox via various fiber or textile fabrication methods to obtain woven or nonwoven aerogels with different structural and mechanical properties to overcome the current limitations of polysaccharide-based aerogels, such as poor mechanical properties and undeveloped shaping techniques. Hereby, a high viscous solution of microcrystalline cellulose and zinc chloride hydrate was wet spun to produce mono and multi-filament alcogel microfibers. Subsequently, cellulose aerogel fibers (CAF) were produced and impregnated with model drugs using supercritical CO_2 processes. Fibers were characterized in terms of morphology and textural properties, thermal stability, mechanical properties, and in vitro biological and drug release assessments. Loaded and non-loaded CAFs proved to have a macro-porous outer shell and a nano-porous inner core with interconnected pore structure and a specific area in the range of 100–180 m^2/g. The CAFs with larger diameter (d ~ 235 μm) were able to form knitted mesh while lower diameter fibers (d ~ 70 μm) formed needle punched nonwoven textiles. Humidity and water uptake assessments indicated that the fibrous structures were highly moisture absorbable and non-toxic with immediate drug release profiles due to the highly open interconnected porous structure of the fibers. Finally, CAFs are propitious to be further developed for biomedical applications such as drug delivery and wound care.

1. Introduction

There is a growing demand for nonwoven and woven materials that are mainly fabricated from petroleum-based resources; however, numerous research studies are trying to fabricate new value-added, sustainable, and competitive products originating from renewable materials such as cellulose [1–3]. Textile engineering is offering a multi-scale toolbox via various fabrication methods of fibers and fabrics for versatile biomedical applications. The current biomedical fibrous structures having a wide range of morphology, composition, and functionality are used in different applications, such as personal protective textiles, skin grafts, tissue engineering scaffolds, and wound dressings [3,4]. The high sensitivity of biomaterial and pharmaceutical agents to the processing condition requires the development of innovative technologies for processing and treatments. Mild temperature supercritical carbon dioxide ($scCO_2$) processes are currently utilized to produce highly porous and low-density material so-called aerogels [1,5]. Cellulose aerogels (CAs), due to their biocompatibility and biodegradability as ultra-lightweight material with 3D interconnected porous network structure, have been used in drug delivery [6,7], tissue engineering [8,9], and wound healing [10,11] applications.

CAs are typically fabricated in three steps: dissolving or dispersing cellulose, gel formation and aging followed by drying, which can be freeze-drying or $scCO_2$ drying. In the latter case, the 3D structure of the gel is merely retained [12,13]. The CAs are also suitable candidates to be loaded with various bioactive agents. Three aerogel impregnation processes have been evolved for loading drugs and bioactive agents, which are the incorporation of the drug to the dissolving mixture before the gelation (gel formation), the addition of the drug through the aging step (solvent exchange), and the inclusion of drug during adsorption/

* Corresponding author at: Aachen-Maastricht Institute for Biobased Materials (AMIBM), Faculty of Science and Engineering, Maastricht University, Brightlands Chemelot Campus, Urmonderbaan 22, 6167 RD Geleen, the Netherlands.
E-mail address: Samaneh.ghazanfari@maastrichtuniveristy.nl (S. Ghazanfari).

https://doi.org/10.1016/j.msec.2021.112196
Received 5 March 2021; Received in revised form 10 May 2021; Accepted 15 May 2021
Available online 20 May 2021

precipitation in the dried aerogels (post-treatment) [11,29]. The solubility of the drug in the gel solvent and $scCO_2$ plays an important role in selecting the right impregnation technique.

Despite CAs outstanding properties, these bioaerogels typically suffer from poor mechanical properties as well as undeveloped fiber processing methods which have limited their shape mainly to monoliths [14,15], cylinders [16,17], and beads/microparticles [9,18,19]. The main limiting factor to produce fibers from most of the bio-based polymers, such as cellulose, is that they do not melt due to the existence of strong hydrogen bonding between macromolecule chains. These hydrogen bondings increase the melting point over the degradation temperature; therefore, processing these raw materials into fiber and finally textile requires dissolution, extrusion, gelation/solidification, and drawing.

Wet spinning is a method for the efficient fabrication of solid/gel fibers from cellulose solutions. Wet spun cellulose fibers often lead to microfibers with better mechanical properties than nanofibers fabricated by electrospinning [20]. In wet spinning, cellulose solution is pumped through a spinneret. Solid/gel fibers are formed when the stream reaches the coagulation bath and are subsequently drawn and collected on a bobbin. Inorganic salt melt hydrates, such as $ZnCl_2$ aqueous solution, are proved to be low-cost, non-derivatizing, and direct solvents for spinning cellulose [21–23]. Therefore, shaping CAs into fibers or filaments is appealing since utilizing textile fabrication methods can transform the fibers into woven, knitted, braided, or nonwoven fibrous structures that hold various structural and mechanical properties.

In literature, there are few studies on wet spun aerogel microfibers production from cellulose [23–27], silk fibroin [28,29], Kevlar [30], polyacrylonitrile [31], silica [32], and graphene [33,34] for versatile fields including thermal insulation, sensors, and flexible batteries and cells. In addition, recently Batista et al. fabricated alginate-chitosan aerogel fibers via emulsion gelation for wound healing applications [35]. Nevertheless, to the best of our knowledge, the usage and potential of wet spinning and textile formation of aerogel fibers for biomedical applications specifically from biobased materials, such as cellulose, have not been investigated. Furthermore, different drug loading techniques, drug-eluting behavior, release kinetics, and biological properties of the CAFs have not been studied.

In this study, the CAFs production with two different diameters from high viscose salt melt hydrate of $ZnCl_2$ (8.3 wt%), fabricated by knitting and nonwoven textile formation, and impregnated with drug models has been investigated. Moreover, the effect of physio-chemical structure of microcrystalline cellulose (MCC) and CAFs, processing parameters such as the effect of $scCO_2$ depressurization rate, and the type of alcohol used for the regeneration of the fibers on the textural properties of the aerogels were studied. Solvent exchange and post-treatment impregnation processes using $scCO_2$ were investigated for loading of the drug models, methyl blue (MB), rhodamine B (RB), and fluorescein (FL).

MB is a triphenylmethane acid dye with antiseptic properties which can be utilized as a fluorescent probe, biological staining agent, and pH indicator [36]. RB and FL are well-known fluorophores which have been used as tracer diagnostic tools and labeling agent in the biomedical field [37–39]. Also, the difference between the polarity, molecular weight, water solubility, and chemical structure of the drug models could provide a closer description of appropriate solute/solvent systems and loading techniques to load other bioactive agents within CAFs. After the solvent exchange drug loading, drug release from the CAFs was measured over 24 h. The release data were rationalized with the kinetics models such as first-order and Peppas-Sahlin in order to define the mass transport mechanism of the drug release. In the end, in vitro assessments were performed to explore cytotoxicity, biocompatibility, and the interaction of the cellulose aerogel fibrous structures with the fibroblast cells.

2. Material and methods

2.1. Materials

MCC with product number C6288 (degree of polymerization of 159), MB, cell proliferation kit II (XTT assay), and propidium iodide, as fluorescent cell staining, were obtained from Sigma-Aldrich. Calcein, a fluorescent probe for staining viable cells, was purchased from Biomol. Gibco™ Dulbecco's modified Eagle's medium (DMEM) with 10% Gibco™ fetal calf serum (FCS) were bought from Thermo Fisher Scientific. $ZnCl_2$ (97%), RB and FL were purchased from Alfa Aesar. For regeneration and washing the fiber samples, absolute isopropanol (iPrOH) (≥99,7%, 2-Propanol CP) and ethanol (EtOH) from Biosolve were used. Carbon-dioxide (CO_2) cylinders (2.7 grade, 50 L) with a purity of 99.7% from Linde Gas Benelux were used in the drying process. Finally, all materials were used without further purification.

2.2. Solution preparation

The MCC was dried at 100 °C in a vacuumed oven overnight to remove the moisture and achieve a constant weight. Spin dopes were prepared using 60% zinc chloride (36 g), 31.66% deionized water (19 mL), and 8.33% microcrystalline cellulose (5 g). First, half of the deionized water was added to swell the cellulose chains and avoid agglomeration during mixing with the salt; subsequently, $ZnCl_2$ salt and the rest of the deionized water were added to the wet powder. Homogenous clear solutions were obtained by dissolving the cellulose at 70 °C and using a mechanical stirrer (100 rpm) after an approximate time of 45 min. Furthermore, two additional lower cellulose concentration solutions (3 and 6 wt%) were similarly prepared to inspect the effect of concentration increment on the cross-sectional morphology of the fibers by scanning electron microscopy.

2.3. Fiber spinning, gel washing, and textile fabrication

The spinning was carried out by a customized wet-spinning "LabLineCompact" unit (DIENES Apparatebau GmbH, Germany) (Fig. 1A-I). To reduce the viscosity, the spinning dope required to be spun at an elevated temperature around 70 °C; therefore, three heaters with suitable controllers were added to the tank, pump, and nozzle pipe. The air pressure (2–3 bar) and pump rate (1.5 mL/min) were applied during the spinning of the multifilament alcogel fibers (spinneret capillary diameter = 100 μm, 100 holes) (Fig. 1A-II) and the monofilament alcogel fibers (spinneret capillary diameter = 330 μm) (Fig. 1A-III). The spinning dope (50 mL) was added to the tank, and the fibers were spun in the iPrOH bath (30 L) without passing through an air gap between the nozzle and the regeneration bath. A customized winder was designed and placed directly in the regeneration bath to prevent alcogel fibers from drying (Fig. 1A-IV).

Alcogel fibers were pulled and winded in the bath at the rate of 20–25 rpm. The wet spun fibers were transferred into a beaker containing fresh iProH. Moreover, to remove the residual salt from fibers and avoid excessive solvent consumption, fibers with their bobbins were placed in cellulose thimbles and washed in a customized soxhlet extractor system (NS 100) (Fig. 1B-I). The extractor pipe (siphon return line) was designed 3 cm above the lowest part of the extraction chamber to keep a reasonable amount of solvent in the chamber and avoid gel drying during the periodical emptiness of the thimble. The presence of salt left-overs was checked by conductivity meter and spot test (Fig. 1B-II). The spot test was performed with silver nitrate (1% wt/v) since acidified Ag^+ gives a white curdy precipitate with Cl^-.

The textiles were formed manually; knitted meshes were created by using a knitting loom and monofilament fibers, and needle punched nonwoven was produced by 3 felting needles purchased from Panduro (coarse, medium, and fine needles, each 7.5 cm long) with a needle base (8 × 10 × 1.8 cm, L × W × H) to punch the multifilament fibers.

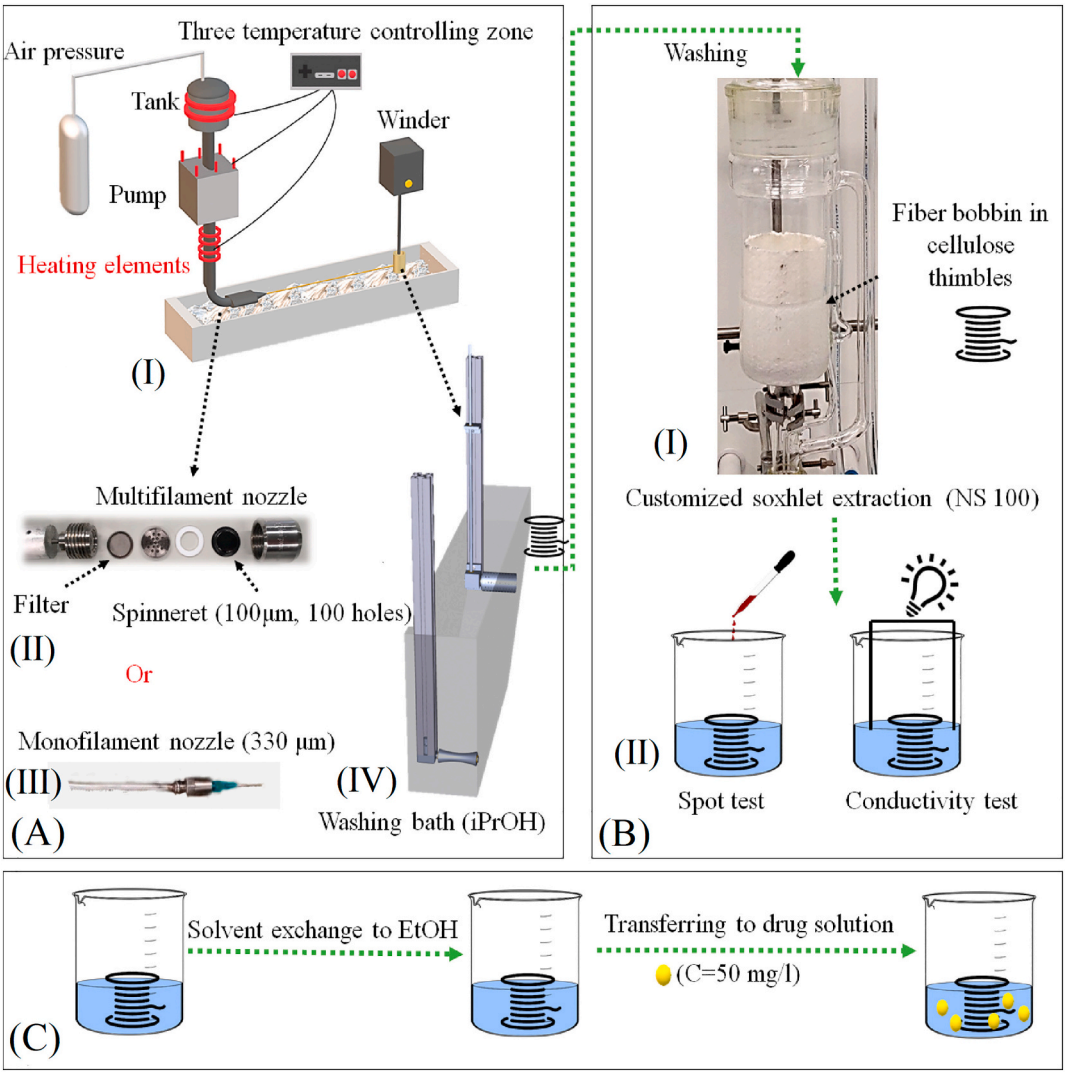

Fig. 1. Schematic representation of wet spinning and fabrication of the salt-free alcogel fibers. (A) Wet spinning and designed components, (I) customized wet spinning line with heating elements, (II) multifilament nozzle with the filter and the spinneret containing 100 holes of 100 μm, (III) monofilament nozzle with an internal diameter of 330 μm. (IV) A custom made winder to collect the alcogel fibers within the bath to avoid drying of the alcogel fibers. (B) Washing process of the alcogel fibers using fresh iPrOH, (I) a customized soxhlet extraction (NS 100) loaded with cellulose thimbles containing alcogel fiber bobbins, (II) evaluation of the salt leftover in alcogel fibers using spot test and conductivity test. (C) Solvent exchange impregnation process of alcogel fiber by immersing them in 50 mg/l drug solutions.

2.4. Supercritical CO_2 drying and drug loading

2.4.1. Supercritical CO_2 drying

The drying procedure was performed using $scCO_2$ dryer HPE 300 (EUROTECHNICA GmbH, Germany). The fabricated alcogel fibers were wrapped in the filter papers and placed in the drying vessel (V = 400 mL) with a defined excess amount of iPrOH. Samples were dried at 120 bar and 50 °C over 60 min. During the drying process, the extraction valve of the vessel was manually opened to vent the alcohol-rich mixture of CO_2 into a plastic flask while the pressure and temperature of the vessel remained constant. The extraction cycle of the alcohol-rich stream was repeated 5 times for a duration of 3 min each. In the end, the vessel was depressurized in 10 min using a backpressure regulator, and the vessel was opened when it cooled down to room temperature. The CAFs were instantly placed in a tightly sealed sample holder under dry N_2 purge to prevent the samples from absorbing the moisture of the environment.

2.4.2. Drug loading

For the impregnation of MB, RB and FL (Fig. S1A) by the solvent exchange step, salt-free alcogels in iPrOH were washed with absolute EtOH in a 1 L beaker two times since the aforementioned model drugs had very low solubility in iPrOH. 50 mg of each model drug was dissolved in 1 L of EtOH, and the solution was stirred at 50 °C with a rate of 200 rpm for 24 h. Around 500 mg of each alcogel fiber was immersed in 2 L of the drug solution and stirred at 50 rpm for 24 h so that the drug could diffuse into all gel bodies (Fig. 1C). In the next step, drug-loaded alcogel fibers were wrapped in the filter paper and transferred to the vessel (V = 100 mL) of the $scCO_2$ dryer. A defined excess amount of the same drug solution for each sample was added to the vessel to prevent ambient drying of the alcogels and $scCO_2$ drying was performed similarly to the unloaded CAFs.

For the post-treatment impregnation of dried aerogels with the model drugs, 25 mg of each drug was placed at the bottom of the high-pressure vessel (V = 100 mL) with a magnetic bar. Then, 100 ± 10 mg of the dried aerogel fibers wrapped in filter papers were placed inside a porous cylinder that had a gap with the bottom of the vessel to avoid any contact between the fibers and the drug powders containing a rotating magnetic bar. A magnetic stirrer was placed under the vessel, and the pressure and temperature of CO_2 were set at 200 bar and 50 °C. After 24

h, the vessel was depressurized over 60 min.

2.5. FTIR

Fourier Transform Infrared (FTIR) spectroscopy was performed on the MCC and the fibers with a frontier FT-IR/NIR (Perkin Elmer, USA), and the spectrum was averaged over 32 spectra with a resolution of 2 cm^{-1} from a range of 4000 till 500 cm^{-1} in the reflectance mode.

2.6. XRD

Two-dimensional (2D) wide-angle X-ray diffraction (WAXD) analysis on samples was performed using a Ganesha diffractometer (SAXSLAB, Denmark) with a sample-to-detector distance of 116.536 mm. Cu Kα radiation (λ = 1.5406 Å) and silver behenate (d_{001} = 58.380 Å) used for calibration were measured for 600 s. The diffraction spectrum was shown by the θ-2θ geometry.

The crystallinity index percentage (CrI (%)) was determined by the empirical estimation method of Segal et al. [40] as the percentage of crystalline material in the sample expressed by the following equation:

$$\mathrm{CrI}(\%) = \frac{I_{002} - I_{am}}{I_{002}} \times 100 \quad (1)$$

where for cellulose I, I_{002} is the maximum intensity of the (0 0 2) lattice diffraction at 2θ ≈ 22.6° and I_{am} is the intensity at 2θ ≈ 18.7° representing the amorphous part in the cellulose fibers. For cellulose II, I_{002} and I_{am} is the intensity at 2θ ≈ 20° and 16°, respectively.

2.7. Thermal gravimetric analysis

The thermal stability and degradation of the MCC and loaded and non-loaded fibers were studied by a TA Q500 thermo-gravimetric instrument (TA Instruments, USA). Samples were heated from 20 °C to 500 °C with a rate of 10 °C min^{-1} under N_2 purge.

2.8. Scanning electron microscopy and micro-computed tomography

2.8.1. Scanning electron microscopy (SEM)

Micrograph images of the CAFs' cross-sections and surface were acquired by Teneo scanning electron microscope (Thermo Fisher Scientific, USA). All fibers were broken in liquid nitrogen and coated with a 3 nm thick layer of iridium. Images were obtained using 5 kV voltage at a working distance of 10 mm. SEM images were analyzed using Image J (version 1.8.0_172, NIH, USA).

Linear shrinkage ΔL of samples was determined from the SEM images by measuring the diameter of the samples after spinning (D_i) and after drying (D_f) using Eq. (2):

$$\Delta L\ (\%) = \frac{D_i - D_f}{D_i} \times 100 \quad (2)$$

2.8.2. X-ray microtomography (μ-CT)

Stack images were obtained using Skyscann 127211MP (Bruker, USA) at the source voltage and current of 40 kV and 200 μA, respectively, with an exposure time of 1.5 s and the image pixel size of 0.8 μm. A CTAn analyzer (version 1.18.8.0+) was utilized to calculate the macroporosity from 2D aerogel structures within three different regions of interest for each sample. In order to visualize 3D images of the samples, CTvox software (version 3.3.0 r1403) was used.

2.9. Textural properties (porosity, surface area, and pore volume)

2.9.1. Porosity

The porosity (∅) was estimated from the bulk density and skeletal density as follows:

$$\varnothing(\%) = \frac{V_{pores}}{V_{material}} = 1 - \frac{\rho_{bulk}}{\rho_{skeletal}} \times 100 \quad (3)$$

where the skeletal density ($\rho_{skeletal}$) of cellulose is 1.501 g/cm^3 [41], and the bulk density ($\rho_{density}$) was estimated as the mass to volume ratio of the three small cylindrical samples. The samples' diameters and lengths were in the range of 1.8–2 mm and 2.3–2.7 mm, respectively. The dimension of the samples was measured by a digital vernier calipers.

2.9.2. Surface area and pore volume

The specific surface area of the CAFs was measured by using the Nova 4200e Surface Area Analyzer (Quantachrome GmbH and Co. KG, Germany). The samples were degassed at 80 °C over 24 h, and the Brunauer–Emmett–Teller (BET) method was utilized to determine the specific surface area (SA_{BET}). Moreover, the pore size distribution and average pore size were obtained from the Barrett-Joyner-Halenda (BJH) model.

2.10. Mechanical properties

The linear density, tensile strength, and elongation measurements of the CAFs were performed using Textechno Favimat+ single fiber testing machine (Herbert Stein GmbH & Co., KG, Germany). The device was equipped with a load cell of 210 cN, and the linear density and tensile measurements were carried out at the rate of 10 mm/min. To address the coarse structure of the fibers and the resulting stiffness, high gauge lengths (20 mm) and high pretensions (1cN/tex) were used.

2.11. Humidity absorbance and water uptake

2.11.1. Humidity absorbance

Three replicates of CAFs (each 100 ± 10 mg) with two different diameters were dried in a vacuum oven at 90 °C around 24 h to reach a constant weight. Subsequently, they were placed for 24 h in a humidity chamber at 25 °C with relative humidity (RH) of 50% and 80%. The weight of the samples was instantly measured before (W_{oven}) and after keeping it in the humidity chamber ($W_{chamber}$). Humidity absorbance weight ratio ($W_{RH\%}$) was measured by:

$$W_{RHX\%} = \frac{W_{chamber} - W_{oven}}{W_{oven}} \times 100 \quad (4)$$

$W_{RH\%}$ is the weight ratio of the absorbed humidity at the relative humidity of (X), (W_{oven}) is the weight after drying the CAFs in the vacuum oven and $W_{chamber}$ is the weight of the fibers after removing from the humidity chamber.

2.11.2. Water uptake

The water uptake was measured after 1, 8, and 24 h and performed on the knitted mesh and nonwoven patches in the PBS solution (pH 7.4, 37 °C) to avoid single fibers breakage and agglomeration. The weight of the swollen samples (W_{wet}) was measured after removing excess water with filter paper for each time point utilizing three replicates. The water uptake weight ratio (WU) (%) was calculated as follows:

$$\mathrm{WU}(\%) = \frac{W_{wet} - W_{oven}}{W_{wet}} \times 100 \quad (5)$$

2.12. In vitro drug loading efficiency, release, and kinetics

2.12.1. Drug loading efficiency

In order to calculate the drug loading efficiency of the solvent exchange impregnation, several assumptions were taken into account. It was assumed that fibers had perfect cylindrical shapes, and the alcogel fiber volume was mainly equal to the ethanol volume since ethanol filled up the majority of the gel matrix. Furthermore, it was assumed that the diffusion of the drugs into the alcogel fibers was complete, meaning that

the concentration of the drug in the solution was equal to that in the alcogel fiber ($C_{alcogel} = C_{ethanol}$) and the drug mass loss during $scCO_2$ drying was negligible. The theoretical drug dose (M_{theo}) can be then expressed as:

$$M_{theo}(\mathrm{mg}) = V_{alcogel}(\mathrm{cm}^3) \times C_{ethanol}\left(\frac{\mathrm{mg}}{\mathrm{cm}^3}\right) \quad (6)$$

Experimental drug doses (M_{exp}) were obtained after washing 100 ± 10 mg of the fibers using 1 L of ethanol in a soxhlet extraction system for 72 h and subsequently measuring the concentration of the drug in the final solution. Drug loading efficiency (%), aerogel loading capacity (wt %), and aerogel specific loading (mg/m^2) can be defined as:

$$Drug\ loading\ efficiency\ (\%) = \frac{M_{exp}\ (\mathrm{g})}{M_{theo}(\mathrm{g})} \times 100 \quad (7)$$

$$Aerogel\ loading\ capacity\ (\mathrm{wt}\%) = \frac{M_{\exp}(\mathrm{g})}{M_{aerogl}(\mathrm{g})} \times 100 \quad (8)$$

$$Aerogel\ specific\ loading\ \left(\frac{\mathrm{mg}}{\mathrm{m}^2}\right) = \frac{Aerogel\ loading\ capacity\ (\mathrm{wt}\%)}{Specific\ surface\ area\ \left(\frac{\mathrm{m}^2}{\mathrm{g}}\right)} \times 1000 \quad (9)$$

The drug loading efficiency of the post-treatment method (in $scCO_2$) was obtained by measuring the weight of the aerogel fibers before (M_i) and after (M_f) the impregnation as expressed by:

$$Drug\ loading\ efficiency\ (\%) = \frac{M_i\ (\mathrm{g})}{M_f(\mathrm{g})} \times 100 \quad (10)$$

Nevertheless, the drug loading efficiency of the post-treatment method was very low (0.01%) and the drugs were slightly adsorbed only on the surface of the fibers. Thus, the post-treatment loaded fibers were not investigated in further characterization steps.

In the result and discussion part, the CAF samples were named as ($F_{diameter\text{-}solvent\ or\ drug}$) in which the subscript refers to the wet spun initial diameter of the nozzle, the final solvent before drying, and the type of the drug that the fiber was loaded with. Table 1 summarizes the fabricated samples and their corresponding abbreviation and characteristics.

2.12.2. Drug release

100 ± 10 mg of drug-loaded CAFs were immersed in 100 mL PBS solution (pH = 7.4) at 37 °C and stirred at a rate of 50 rpm. 16 samples over 24 h at various time intervals were measured as follows: 2 mL from the PBS and sample solution was transferred into a vial and subsequently, 2 mL of fresh PBS was added to the solution to maintain a constant medium volume. The measurements were performed in triplicate. Using a UV–visible UV3600 spectrophotometer (Shimadzu, Japan), the maximum absorption peaks for MB, RB, and FL in PBS solution were at the wavelengths of 306, 554, and 490 nm, respectively.

The blank, calibration material, and all the collected samples over time were placed in 96 well plates, and Synergy™ HTX multi-mode microplate reader (BioTek, USA) was used to obtain the intensities. The Beer-Lambert law was utilized to obtain the concentration of the drug, and cumulative drug release was calculated by:

$$Q(\%) = \frac{C_n V + V_i \sum_{i=0}^{n-i} C_i}{M_{exp}} \times 100 \quad (11)$$

Q (%) is the percentage of the cumulative released drug, and V (mL) was the total volume of the samples. C_n (mg/mL) and V_i (mL) were the concentration and the volume of the samples taken at *n* and *i* time points. M_{exp} (mg) was the actual weight of the drug in the fibers, and the number of times that the drug release media was replaced is shown as *n*.

2.12.3. Kinetics of release

First-order and Korsmeyer-Peppas were selected as the mathematical models to fit the experimental data obtained from the drug release measurements from the CAFs since previous drug release studies showed CAs were stable (no erosion) in aqueous media [42]. The correlation coefficient (R^2) was calculated to define the accuracy of each model.

2.12.3.1. First-order. The first-order release kinetics is corresponding to the amount of the loaded drug in the fiber matrix. This model results in a constant release over time, and the rate is only reliant on the initial drug concentration [43,44]. The cumulative released fraction ($Q_{(t)}$) can be described by:

$$Q_{(t)} = 1 - exp(-k_1 t) \quad (12)$$

where ($1 - Q_{(t)}$) represents the remaining fraction of the drug at the time t in the system, and k_1 is the first-order constant.

2.12.3.2. Korsmeyer–Peppas. The Korsmeyer-Peppas, known as the power-law model, explains the exponential relationship between the release and the time [44,45]. The model is expressed by:

$$Q_{(t)} = \frac{M_t}{M_{tot}} = K_{KP} t^n \quad (13)$$

where M_t is the amount of the drug at the time t, M_{tot} is the total amount of the loaded drug, K_{kp} is the constant accounting for the structural and geometrical characteristics of the system, and *m* is the exponent of the release related to the drug release mechanism. This model is limited to the first 60% of cumulative release or Q(%) < 60%. In case of $n < 0.45$, Fickian diffusion takes place by the typical molecular diffusion of the drug due to a chemical potential gradient. When $0.45 < n < 0.89$, the release is controlled by the effect of both diffusion and polymer relaxation (swelling or erosion).

2.13. In vitro cell viability and proliferation studies

Human dermal fibroblasts were isolated from the adult skin biopsies as previously described by Kreimendahl et al. [46]. Cells were cultured at 37 °C and 5% CO_2 in DMEM with 10% fetal calf serum (FCS). Cells at passage 4 were used for the viability and proliferation experiments using XTT and live dead staining. The CAFs samples were sterilized in 70% ethanol and washed in PBS prior to the tests.

XTT assay was performed according to the ISO 10993-12. In short, samples, positive control, and negative control were incubated in a culture medium for 72 h. The negative control was a piece of polyethylene tube, and the positive control was a piece of a latex glove. Cells were seeded in 96-well plates (1×10^4 cells per well) and were allowed to adhere to the wells for 24 h. After 24 h, cell medium was exchanged with sample medium, positive control, and negative control or blank. After different incubation periods of 1, 3, and 7 days, the XTT assay was performed according to the manufacturer's protocol. The absorbance was measured in a multimode microplate reader M200 (Tecan, Switzerland) at 450 nm with a reference wavelength of 630 nm. The

Table 1
Fabricated samples and their labels.

Sample name	Spinning nozzle diameter (μm)	Solvent prior to the $scCO_2$ drying	Type of the loaded drug
$F_{330iPrOH}$	330	Isopropanol	–
$F_{330EtOH}$	330	Ethanol	–
$F_{100iPrOH}$	100	Isopropanol	–
$F_{100EtOH}$	100	Ethanol	–
F_{330RB}	330	Ethanol	Rhodamine B
F_{100RB}	100	Ethanol	Rhodamine B
F_{330FL}	330	Ethanol	Fluorescein
F_{100FL}	100	Ethanol	Fluorescein
F_{330MB}	330	Ethanol	Methyl blue
F_{100MB}	100	Ethanol	Methyl blue

assessment was performed in three replicates.

For the live-dead assay, nonwoven textiles were punched using a biopsy punch and were placed in 96-well plates. Cells were seeded on the textile with a concentration of 5×10^4 cells per well. Live-dead assay on days 1 and 7 was performed according to the manufacturer's protocol as described previously [47]. Images were obtained using an inverted confocal microscope (Leica SP8, Germany).

2.14. Statistical analysis

All the experimental data are expressed as means ± standard errors (SD). The statistical analysis was done by Originlab (2019 b) using a significance level of $p < 0.05$. Student *t*-test and one-way ANOVA based on the Tukey test was performed to determine the differences between different data groups.

3. Results and discussion

3.1. Estimation of cellulose aerogel fibers density and porosity

The salt-free alcogel fibers and cylinders were successfully prepared. After $scCO_2$ drying, white opaque mono and multifilament CAFs (8.3 wt %) were obtained (Fig. 2A-I and II). The bulk density and porosity of the fibers were estimated from the small fabricated cylinders (8.3 wt%) (Fig. 2A-III) as 0.188 ± 0.025 g/cm^3 and 87.5 ± 1.7 (%), respectively. By considering the higher cellulose concentration of the fabricated CA cylinders and comparing them to the reported values for the density of the lower concentration CAs (e.g., 0.14 g/cm^3 for 6 wt%) produced from similar salt melt hydrates, it can be concluded that the obtained density and porosity data are in agreements with previous studies [25,48].

3.2. Structural properties and crystallinity by FTIR and WAXS

3.2.1. Fourier-transform infrared spectroscopy

FTIR spectra of the cellulose powders and fabricated CAFs in the wave number region of 4000–500 cm^{-1} are exhibited in (Fig. 2B). The cellulose spectra showed bands at 3650–3000 cm^{-1} (O—H hydroxyl group stretching vibration), 2900–2800 cm^{-1} (–CH_2– alkyl stretching vibration), 1645 cm^{-1} (C═O stretching), and 1020 (C—O stretching). The presence of numerous intra- and inter-molecular hydrogen bonds between hydroxyl groups organize cellulose chains in a semi-crystalline structure with a low ordered amorphous region in two polymorphy of cellulose I and cellulose II (Fig. 2C-I) [49]. The crystalline structural transformation of cellulose from cellulose I to cellulose II were studied with the investigation of absorption bands at 897, 1107, 1161 and 1430 cm^{-1}, which are attributed to group C_1 frequency, ring asymmetric stretching, C-O-C asymmetric stretching, and CH_2 symmetric bending vibration mainly in cellulose I, respectively.

In addition, the 893 cm^{-1} absorption band (β-glucosidic linkages between the sugar units) confirmed that the crystalline cellulose I can be almost insignificant in the regenerated cellulose fibers since the 893 cm^{-1} is allocated to group C_1 frequency in cellulose II [30,31]. In comparison with the MCC, the CAFs retained the most original FTIR peaks in a broader form, except for the cellulose I peaks, which were

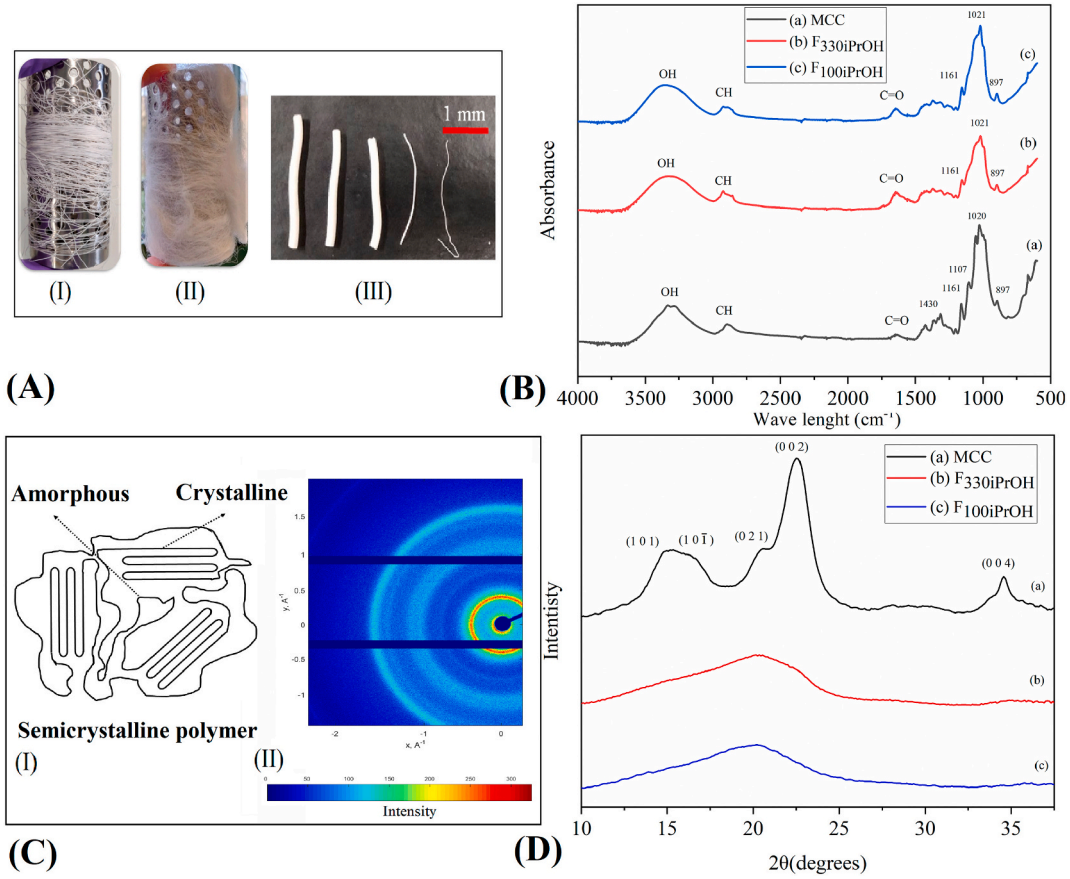

Fig. 2. (A) The macroscopic images of the produced aerogel; (I) CAF_{330}, (II) CAF_{100}, and (III) on the left three small cylinders produced for bulk density measurement and CAF_{330} and CAF_{100} on the right. (B) FTIR spectra of MCC and CAF exhibiting transformation of cellulose I to cellulose II. (C) Crystalline properties of the MCC and the produced fibers; (I) schematic representation of a semicrystalline polymer, (II) the detector image of the MCC exhibiting high crystalline regions (the color bar indicates the intensity of the adsorbed radiation, low is blue and high is red). (D) XRD pattern of the MCC and the CAFs proving amorphous structure of the CAFs and the highly crystalline structure of the MCC. (For interpretation of the references to color in this figure legend, the reader is referred to the web version of this article.)

mainly vanished or decreased significantly. Besides, to ensure that the salt-free CAFs were produced, no chlorinated compound peaks were observed [50,51]. The peaks from CAF_{EtOH} and CAF_{iPrOH} were similar. Furthermore, the FTIR spectra of the drug-loaded CAFs showed a similar pattern to the CAF_{EtOH} (Fig. S1B, C, and D). However, the main bands of the drug models, such as -OH, C═O, and phenolic C—O stretching's, could not be observed in the FTIR spectrum of the loaded CAFs due to the overlapping with cellulose bands. The low intensified shoulders in the wavelength range of 700–1000 cm^{-1} can prove the presence of drug models in the aerogels.

3.2.2. Wide-angle X-ray scattering

The spectral detector image (Fig. 2C-I) and XRD diffractogram (Fig. 2C-II) of microcrystalline cellulose exhibited five major diffraction peaks at $2\theta = 14.9$ (1 0 1), 15.9 (1 0 $\bar{1}$), 21 (0 2 1), 22.5 (0 0 2), and 34.6 (0 0 4), which are in agreement with values reported in the literature for cellulose [52,53]. The CAFs samples gave a diffractogram which clearly represented an amorphous structure. This character is validated by the absence or notable reduction of all peaks standing for planes (1 0 1) and (0 0 2) as the characteristic peaks of cellulose I. Moreover, the cellulose aerogels diffractogram shows peaks at $2\theta = 13°$ and 20°, which are the corresponding properties of cellulose II [54]. The crystallite index for the MCC, F_{330}, and F_{100} was 81.15, 27.58, and 28.78 (%), respectively. It is important to mention that no effect of the subsequent solvent change from iPrOH to EtOH was observed on the XRD patterns.

The FTIR and XRD indicated a clear conversion of MCC from cellulose I to cellulose II structure with forming aerogel fibers in the amorphous phase. This notable reduction in crystallinity can be interpreted in the modified hydrogen bonding and antiparallel orientation of cellulose chains, which occurred during dissolving the MCC in the salt melt hydrate and led to the continuous transformation of cellulose I into an amorphous state [22].

3.3. Thermal analysis utilizing TGA and DTA

Thermogravimetric analysis (TGA) curves depicted in (Fig. 3A) showed a first decomposition stage in the range of 30–105 °C for the MCC and the CAFs regenerated in iPrOH due to the loss of moisture and other volatile solvents. A second decomposition stage was found in the range of 220–350 °C for the CAFs and 265–350 °C for the MCC, indicating lower thermal stabilities of the fibers. The differential thermal analysis (DTA) curves shown in (Fig. 3B) implies that the CAFs exhibited a slower degradation rate compared to the MCC. No difference between CAF_{EtOH} and CAF_{iPrOH} was observed.

In the TGA profiles, the fibers exhibited greater weight loss in the first absorbance stage, mainly due to interconnected highly porous structure and higher accessibility of hydroxyl groups of the cellulose chains to the water molecules. However, the fibers had slightly lower thermal stability in comparison to the MCC because of the lower crystallinity and degradation of the cellulose chains which occurs during the cellulose dissolving process in salt melt hydrates [22].

3.4. Morphology and structural studies using SEM and μ-CT

3.4.1. Scanning electron microscope

Cellulose aerogels produced in lower concentration (3 wt%) had a randomly oriented nanofibrillar structure (Fig. 4A-I) while increasing the concentration showed nanofibrils agglomeration in the form of "strands" (6 wt%) (Fig. 4A-II). With further increase of the cellulose concentration (8.3 wt%), the strands were condensed and the fibers exhibited lower pore size dimensions (Fig. 4A-III) [17,55]. The knottability of the fibers without fibrillation or breakage of the fiber surface is displayed in Fig. 4B-I.

Open porous surface morphologies of the CAFs with the direction of the fibers are shown in Fig. 4B-II and III. Since there was no air gap between the nozzle and the bath, no film formation occurred on the surface of the CAFs; however, $F_{330iPrOH}$ and $F_{100iPrOH}$ exhibited different surface structures. $F_{100iPrOH}$ displayed a porous surface with elongated pores perpendicular to the fiber axis, while $F_{330iPrOH}$ had more elongated pores in the direction of the fiber axis besides more irregular distribution of the pores on the surface. This dissimilarity in the surface morphology and pores elongation alignment can originate from the spinning nozzle compartments. Monofilament spinneret ($F_{100iPrOH}$) benefited from a more complex spinning pack with conical shape spinneret holes. In particular, the spinning dope passed through the multifilament spinning pack in which filter plates caused fluid breakage and better achievement of gel uniformity before being extruded in the coagulation bath.

The textile structure investigated under the microscope showed that the knitted mesh formed by several loops and knots alongside the fiber axis had no sign of breakage or deformation of the fibers (Fig. 4C-I), and the needle punched nonwoven formed a highly condensed patch (Fig. 4C-II).

The CAFs cross-sections consisted of a macro-porous outer shell and a nano-porous inner core (Fig. 5A-I, II, III, and IV). The CAFs (8.3 wt%) regenerated in iPrOH and ethanol exhibited no specific morphological distinction, and fibers' morphologies were similar to those reported in the CAFs studies [24,25,48]. It is likely that the core-shell structural difference was formed when the hot spinning dope entered the regeneration bath and the alcohol began to vaporize. The alcohol vapor then diffused through the gel matrix and generated macrospores in the shell region and accessible pores on the surface of the fiber. With cooling down the fiber in ethanol, this process terminated and was limited to the

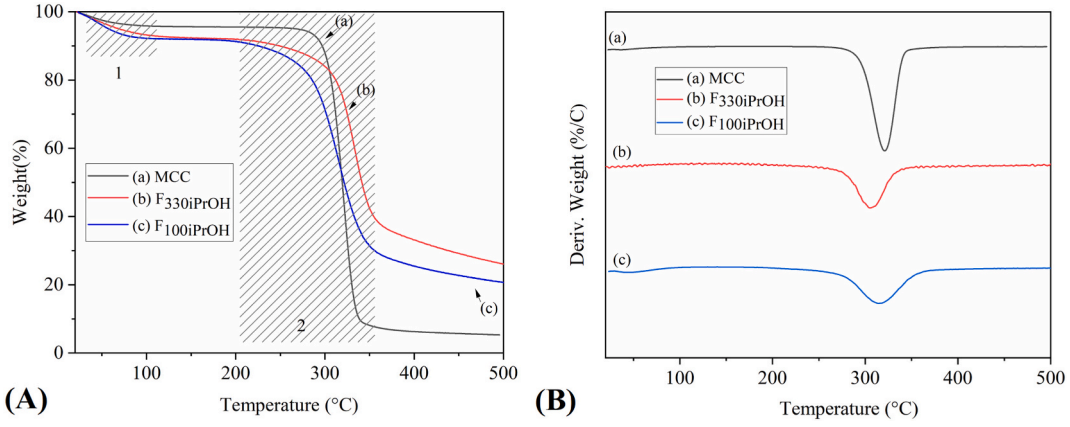

Fig. 3. (A) TGA graphs of the MCC and the CAFs regenerated in iPrOH. The first step (from 30 to 105 °C) in the mass loss was due to the evaporation of water molecules, and the second step at 220–350 °C was the relatively rapid decomposition of the cellulose chains. (B) DTA of the regenerated fibers and the MCC showed that the decomposition range was broader and the rate was slower in the fibers compared to the MCC.

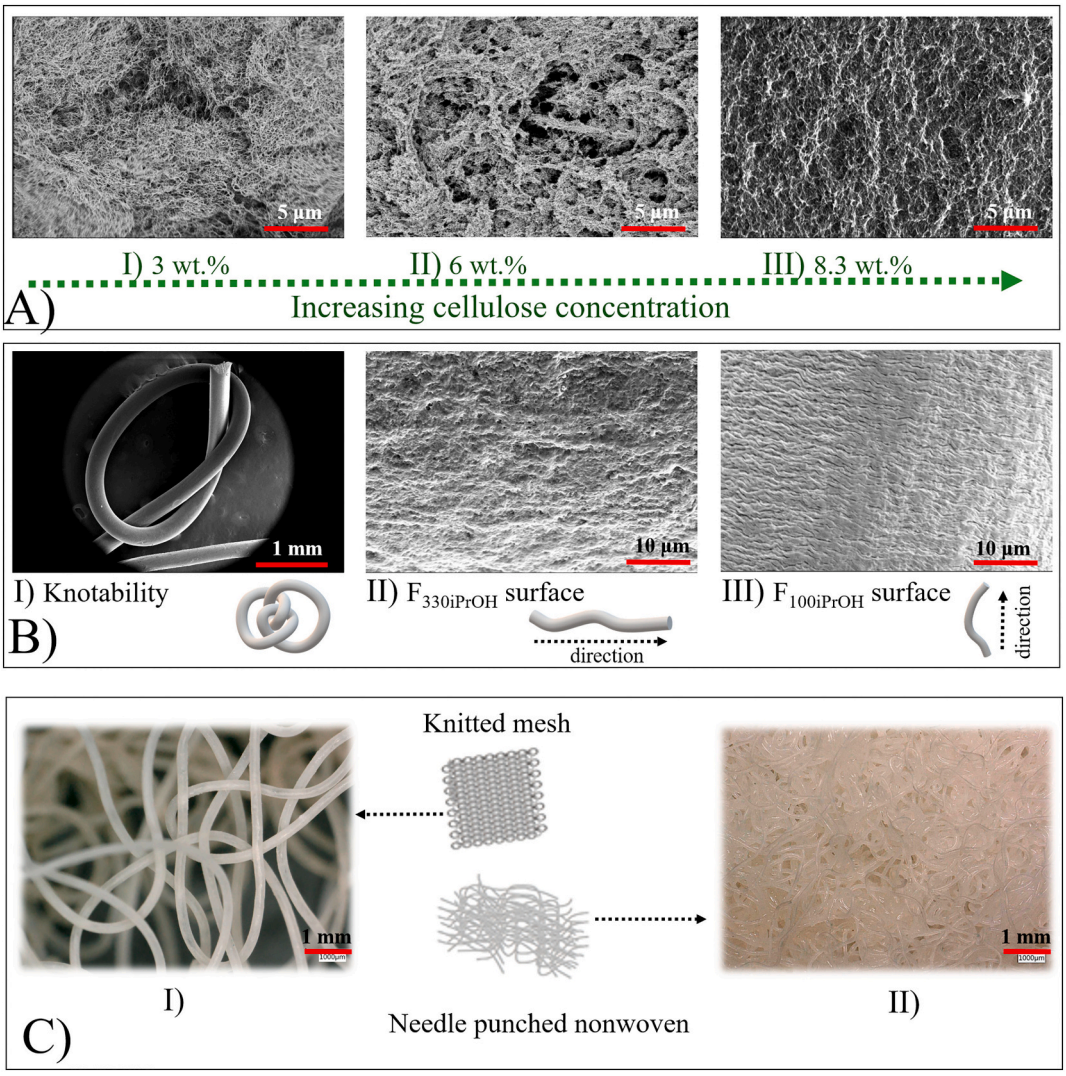

Fig. 4. (A) SEM images of various concentrations of cellulose showed (I) a random nanofibrillated morphology in 3 wt%, (II) strand-like morphology in 6 wt%, and (III) highly condensed structure in 8.3 wt% CAFs with porous structure. (B) The SEM images of the knot made from the F330iPrOH (scale bar 1 mm) (I), (II) porous surface of the $F_{330iPrOH}$ (scale bar 10 µm) alongside the fiber direction, and (III) open surface pores of the $F_{100iPrOH}$ with perpendicular alignment to the fiber axis (scale bar 10 µm). (C) Microscope images of (I) a knitted mesh with several loops and knots of the CAF_{300} (scale bar 1 mm) and (II) a needle punched nonwoven patch (scale bar 1 mm).

outer shell of the fiber. In the fibers with a larger diameter, a slightly larger macro-pore shell is formed as the cooling time is proportional to the fiber diameter. Similar cross-sectional morphology was observed in the fibers impregnated with MB, RB, and FL (Fig. S2). Also, it can be concluded that the solvent exchange impregnation of the drug models did not lead to the significant collapse of the pores and thus its influence on the morphological properties of the fibers is negligible. The total linear shrinkage of the CAFs after gelation, washing, and $scCO_2$ drying steps were 25.1 ± 1.5% and 28.7 ± 1.1% for CAF_{100} and CAF_{330}, respectively.

3.4.2. X-ray microtomography

µ-CT was used to investigate the 3D microporous architecture of the CAFs (8.3 wt%) regenerated in iPrOH (Fig. 5B-I-c and III-g) and those subsequently solvent exchanged to ethanol (Fig. 5B-II-e and IV-i). The reconstructed images of the CAFs volumes indicated that the pores were distributed throughout the fiber matrix. Similarly, defect volume analyses were performed for the CAF_{iPrOH} (Fig. 5B-I-d and III-h) and CAF_{EtOH} (Fig. 5B-II-f and IV-k) estimation of porosity where the macrospores have been divided into three regions of red, green, and blue as an indication of the macrospores size distribution. Detailed information on the percentage of the open and closed pores, the average structural thickness (cellulosic walls between macropores) within the CAFs volume, and the average macrospores diameter calculated from µ-CT image stacks are provided in Table 2.

Overall, the CAF_{330} samples had higher porosity and lower average pore diameter with higher structure thickness than the CAF_{100}, and no significant difference between two regeneration alcohols for the same CAF diameter was observed. However, one might notice the resolution of the µ-CT detector is limited to 0.8 µm, and therefore the pores less than this resolution are not considered in the image stacks calculation. The porosity of the fibers is closer to the porosity obtained from the bulk density in Section 3.1. However, µ-CT is still a very useful tool to investigate the interconnectivity of the pores and the macrospore size distribution within the matrix. For instance, macroporosity is essential for the diffusion of nutrients and gases and the proliferation of cells in biomedical applications such as tissue engineering scaffolds [52]. It is worthy to mention that since aerogels have a broad range (from nm to µm) of morphological characteristics, such as pore lengths and diameters, multiple characterization methods are required to quantify

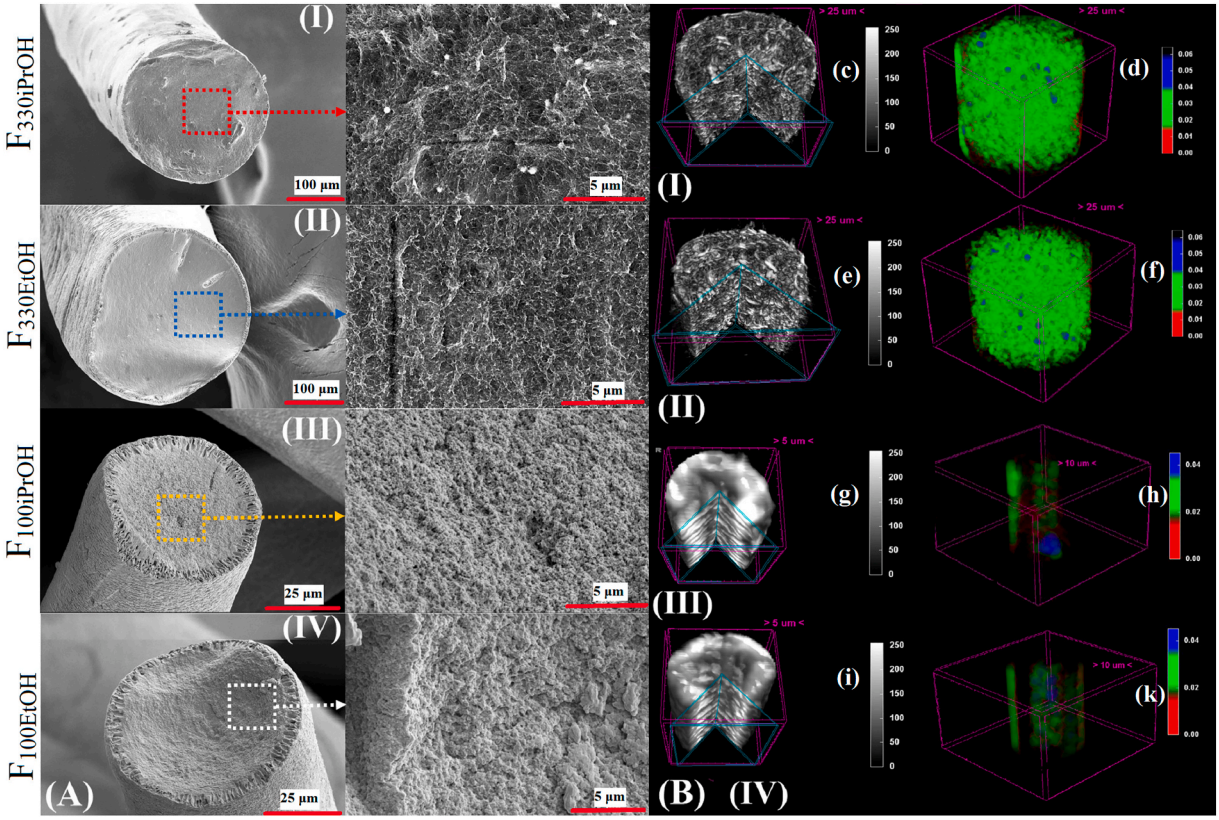

Fig. 5. (A) Cross-sectional morphology of the cellulose fibers exhibiting a macro-porous outer shell with a nano-porous inner core of (I) $F_{330iPrOH}$ and (II) $F_{330EtOH}$ (magnification and scale bars in the left column (100 µm) and right column images (5 µm)) and (III) $F_{100iPrOH}$ and (IV) $F_{100EtOH}$ (magnification and scale bars in the left side (25 µm) and the right side images (5 µm)). (B) µ-CT computed tomography 3D reconstructions of the CAFs with cut prism shape of the volume indicating interconnected porous structure within the whole volume of the fibers; (I-c) $F_{330iPrOH}$, (II-e) $F_{330EtOH}$, (III-g) $F_{100iPrOH}$, and (IV-i) $F_{100EtOH}$. Defect volume analysis for estimation of the porosity where the macrospores have been divided into RGB colors as an indication of the size distribution of the macropores for (I-d) $F_{330iPrOH}$, (II-f) $F_{330EtOH}$, (III-h) $F_{100iPrOH}$, and (IV-k) $F_{100EtOH}$. (For interpretation of the references to color in this figure, the reader is referred to the web version of this article.)

Table 2
The percentage of the open and closed pores, the average structural thickness (cellulosic walls between macropores) within the CAFs volume, and the average macrospores diameter calculated by CTAn software from µ-CT image stacks in different regions of interests.

Sample name	Open porosity (%)	Closed porosity (%)	Structure thickness (µm)	Average diameter of macropores (µm)
$F_{330iPrOH}$	59.0 ± 1.0	0.020 ± 0.001	7.90 ± 0.31	9.51 ± 0.97
$F_{330EtOH}$	56.29 ± 0.99	0.021 ± 0.003	8.51 ± 0.20	10.0 ± 1.4
$F_{100iPrOH}$	38.87 ± 0.94	0.024 ± 0.004	13.05 ± 0.44	7.8 ± 1.4
$F_{100EtOH}$	37.201 ± 0.055	0.031 ± 0.0043	12.87 ± 0.38	6.3 ± 1.9

both nanoscale and macroscale parameters and provide a consistent overall view of the aerogels textural properties. In the next section, for a better understanding of porosity, N_2 adsorption was performed as an additional tool to cover the mesoporosity.

3.5. Textural properties by N_2 adsorption-desorption

The N_2 adsorption-desorption isotherms of the CAFs regenerated in iPrOH and those subsequently solvent exchanged with EtOH are shown in Fig. 6A and B. The CAF_{EtOH} and fibers with thicker diameters absorbed higher quantities of N_2. Nevertheless, the isotherms curves in all samples are similar to IUPAC type IV with a hysteresis loop in the range of 0.7–1.0, representing the presence of meso- and macro-porous structure, which is pursuant to the SEM and µ-CT results [56].

The multi-point BET of CAFs specified that the successive solvent exchange to EtOH enhanced the SA_{BET} in the CAF_{100} and CAF_{300} (Fig. 6C). The $CAF_{330EtOH}$ (177 ± 16 m^2/g) had significantly higher SA_{BET} than the $CAF_{100EtOH}$ (103 ± 5 m^2/g). The solvent exchange drug loading of the fibers did not have a significant impact on the SA_{BET} of the drug-loaded CAF_{330} samples but the results were rather different in the drug-loaded CAF_{100} (Fig. 6D). Lower diameter fibers impregnated by FL and MB showed significantly lower SA_{BET} in comparison to the CAF_{330} and RB loaded CAF_{100}. The relative SA_{BET} data of the CAFs and the loaded CAFs are shown in Table 3.

The BJH revealed that the size of nanopores was mainly distributed between 5 and 20 nm in all samples (Fig. 7A). The pore volume of the $CAF_{330EtOH}$ (1.055 ± 0.142 cm^3/g) was not significantly different from the $CAF_{330iPrOH}$ (0.765 ± 0.150 cm^3/g). However, the higher fiber diameter exhibited higher pore volume than lower diameter fibers, indicating the effect of the fiber thickness on the pore volume (Fig. 7B). All average pore diameter and pore volume data of the pure and drug-loaded CAFs are shown in Table 3.

The subsequent solvent exchange from iPrOH (relative polarity of 0.546) to more polar alcohol EtOH (0.654) increased the SA_{BET} of the fibers. The observed increase in the SA_{BET} could be attributed to EtOH higher polarity causing fibrils linking zones to disintegrate and release loosely packed fibrils from the alcogel body [48,57]. Moreover, the pore volume difference in the CAF_{330} samples with the CAF_{100} can be explained based on the fact that the CAF_{330} nano-porosity (core) to macro-porosity (shell) ratio was higher than that of the CAF_{100} due to the higher diameter of the fibers during fiber regeneration and alcohol

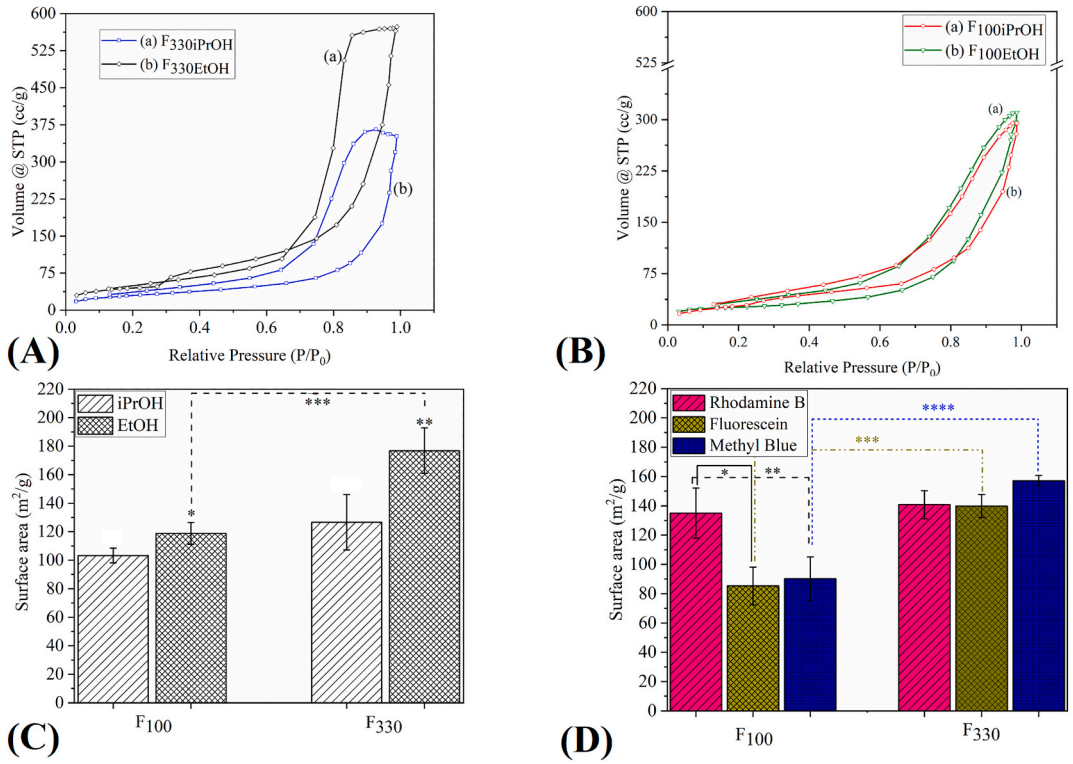

Fig. 6. The N_2 adsorption-desorption isotherm curves of the CAFs regenerated in iPrOH (A) and solvent exchanged to EtOH (B). (C) The surface area of CAF_{100} and CAF_{300} regenerated in iPrOH and solvent exchanged to EtOH. (D) The surface area of rhodamine B (RB), fluorescein (FL), and methyl blue (MB) loaded CAFs by solvent exchange impregnation. In all diagrams (* data statistically significant $p < 0.05$).

Table 3
The surface area (m^2/g), pore volume (cm^3/g), and average pore diameter (nm) of the non-loaded and loaded CAFs.

Sample name	Surface area (m^2/g)	Pore volume (cm^3/g)	Average pore diameter (nm)
$F_{330iPrOH}$	127 ± 19	0.77 ± 0.15	9.285 ± 0.037
$F_{330EtOH}$	177 ± 16	1.06 ± 0.14	11.625 ± 0.055
$F_{100iPrOH}$	103 ± 5	0.522 ± 0.012	7.157 ± 0.066
$F_{100EtOH}$	119 ± 8	0.544 ± 0.074	7.099 ± 0.042
F_{330RB}	141 ± 9	0.927 ± 0.051	11.6 ± 2.3
F_{100RB}	135 ± 17	0.472 ± 0.060	7.106 ± 0.012
F_{330FL}	140 ± 8	0.871 ± 0.035	7.5 ± 5.2
F_{100FL}	85 ± 13	0.371 ± 0.047	13.75 ± 0.17
F_{330MB}	157 ± 4	0.939 ± 0.032	10.9 ± 1.3
F_{100MB}	90 ± 15	0.412 ± 0.057	8.6 ± 1.3

evaporation as discussed in Section 3.4.

In the end, the effect of depressurization time over 10, 20 and 60 min on the fabricated samples were explored and no significant effect on the textural properties of the CAFs was observed; though, depressurization time of less than 10 min could cause freezing of the samples and further collapsing of the pores due to the fast expansion of CO_2 within the vessel.

It should be noted that due to the variation in the BET and BJH data, these data must be interpreted with caution since there are some challenges within the sample preparation and measurements. For instance, aerogel fibers were very lightweight with high electrostatic charges. In order to add enough weight of the aerogel fibers to the measurement tube, the aerogel fibers had to be densely filled in the test tube. Since controlling this process was hard, there might be some extent of compression when samples were filled in the test tube.

3.6. Mechanical properties

Fig. 8A represents the amount of forces that the CAFs with two different diameters could withstand. The CAF_{330} fibers could withstand greater forces (159 ± 14 cN) than the CAF_{100} samples (6.9 ± 1.6 cN) due to their larger diameter. Fig. 8B shows the representative curves of tenacity versus elongation (%) with an indication of data spread for the maximum tenacity (cN/dtex) and maximum elongation (%) of the CAF_{330} and CAF_{100} samples. The aerogel fibers had similar behavior to the previously reported studies on cellulose aerogel fibers in which a linear regime was followed by an irreversible plastic deformation until the fracture happened [25]. Both fibers showed a wide range of mechanical data, but their maximum tenacity was in close range to each other, 0.34 ± 0.17 and 0.36 ± 0.18 (cN/dtex) for the CAF_{330} and CAF_{100} samples, respectively. The maximum elongation of the CAF_{100} (16.3 ± 4.5%) was significantly higher than the CAF_{300} (9.2 ± 4.5%). It seems likely that the difference in the maximum elongation results arose due to the difference in the stiffness of the samples. One possible explanation could be that the thinner fibers are denser and/or have more strongly connected nanofibrils than thick fibers, as it was also perceived by BJH analysis that the CAF_{100} had lower pore volume than CAF_{300}. Furthermore, the data outspread in both samples could be attributed to several reasons including highly open non-homogeneous distribution of the pores, coarse nature of the fibers, slight diameter variation along the fiber axis, slight residual stiffness during the measurement, misalignment and kinking in the fiber matrix.

3.7. Humidity absorbance and water uptake properties

The CAF_{330} fibers showed a superior moisture weight ratio than the CAF_{100} because of their higher SA_{BET} and pore volume which provided more accessible hydroxyl groups for the water molecules (Fig. 8C). Furthermore, with increasing the relative humidity from 50 to 80% in both samples, the weight ratio of the adsorbed humidity increased from 5.54 ± 0.53 and 7.9 ± 1.1 to 13.54 ± 0.13 and 15.9 ± 1.3 for CAF_{100} and CAF_{330}, respectively.

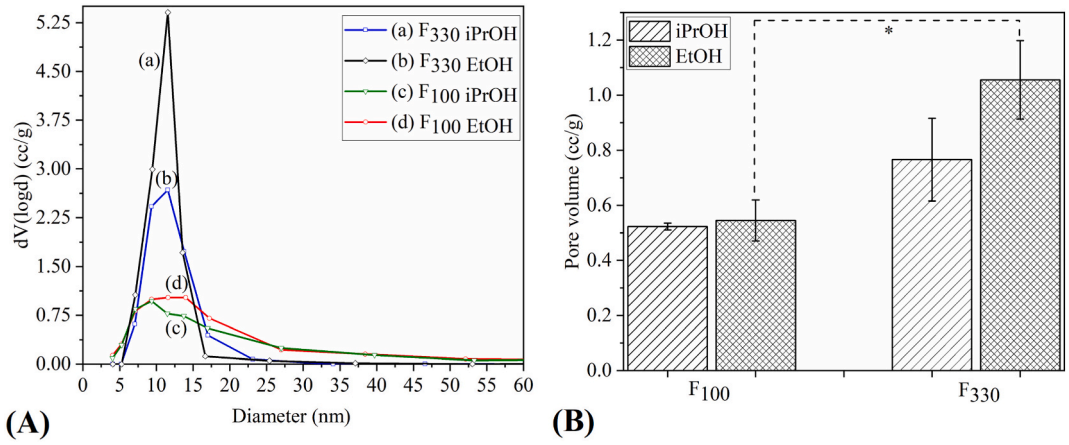

Fig. 7. (A) Representative curves of the pore-size distribution determined by N_2 adsorption-desorption for the CAFs regenerated in iPrOH and those subsequently exchanged to EtOH. Most of the pores were within the range of 5–20 nm. (B) The pore volume of the CAFs, higher diameter fibers exhibited higher pore volume (*$p < 0.05$).

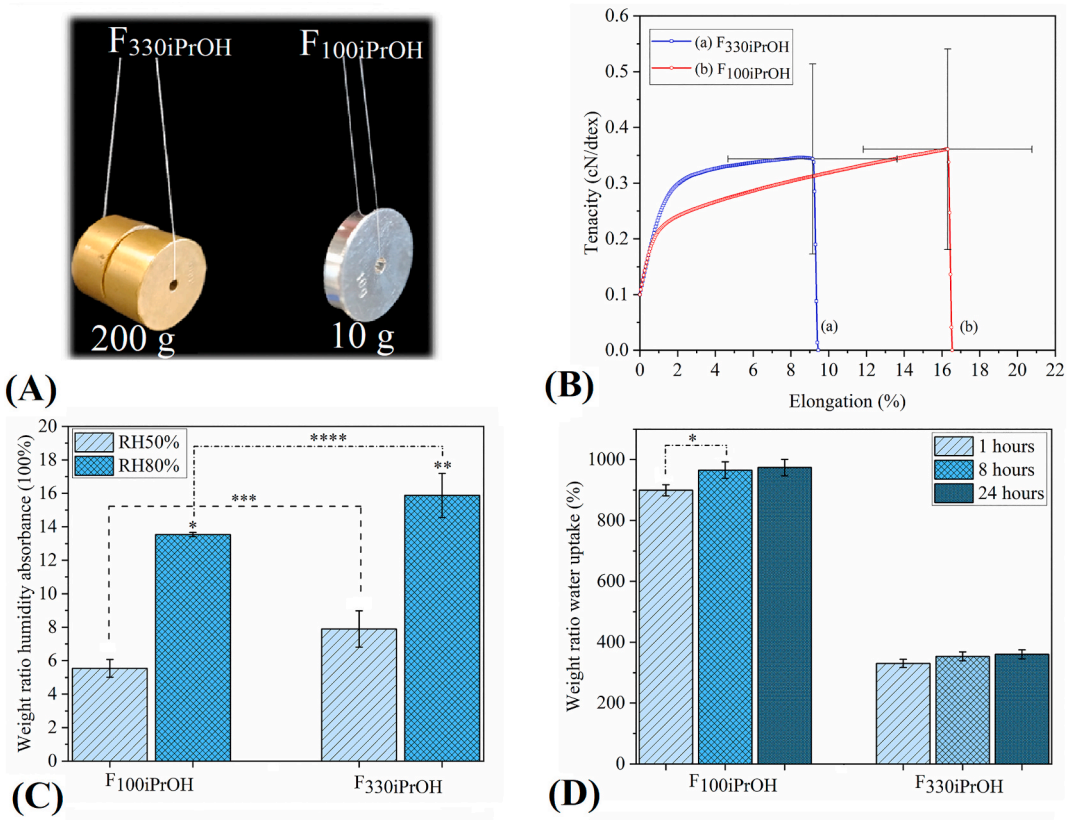

Fig. 8. (A) The $CA_{F330iPrOH}$ holding 200 g and the $CA_{F100iPrOH}$ carrying 10 g weight, fibers with higher diameter withstood higher forces. (B) Representative curves of tenacity-elongation for $CAF_{330iPrOH}$ and $CAF_{100iPrOH}$ with tenacity and the maximum elongation over 20 tensile measurements of the CAFs. $CAF_{330iPrOH}$ and $CAF_{100iPrOH}$ showed very close maximum tenacity (~0.36 cN); however, the CAFs with the lower diameter had higher elongation (~16%). (C) Humidity absorbance of the CAFs within 50 and 80 RH%, the relative humidity in the CAF_{330} was higher and would increase by enhancing the RH%. (D) Water uptake of the knitted and needle punched samples made from $CA_{F330iPrOH}$ and $CAF_{100iPrOH}$ at 1, 8, 24 h. Needle punched samples had superior water uptake capacity up to 1000 wt%.

The water uptake tests (Fig. 8D) indicated superabsorbent property for the nonwoven textile made of the CAF_{100} since 1 g of the cellulose aerogel could absorb around 100 g of water; whereas the water uptake weight ratio of the knitted mesh of CAF_{330} was almost three times lower. This phenomenon was presumably because of the macrostructure of the nonwoven patch rather than textural properties of the fibers as the higher surface to volume ratio of the CAF_{100} within the condensed framework of the needle punched nonwoven can entrap more water molecules compared to the loosely packed structure of the knitted mesh.

3.8. Drug loading, release, and kinetic models

The fibers were loaded during the solvent exchange step and the post-treatment process in $scCO_2$. The theoretical amount of the solvent exchange impregnation using Eq. (6) was estimated to be 5.11 ± 0.19 mg/cm^3 for all samples. The experimental amount of the loaded drug,

calculated drug loading efficiency, aerogel loading capacity, and specific loading of the solvent exchange impregnation for RB, MB, and FL are shown in Table 4. The CAF_{330} samples indicated slightly higher drug loading efficiency than the CAF_{100} samples in all drug models. Aerogel loading capacity and specific loading were in the sequence of RB > MB > FL.

It seems possible that these differences in the drug loading efficiency are due to the interaction and solubility of these molecular probes with the alcohol and the affinity of the drug models with cellulose macromolecules since they can bind to the cellulose chains by electrostatic interactions and hydrogen bonding [58,59]. Furthermore, at a low concentration of the drug (50 mg/L), sorption plays an important role since every hydroglucose unit within cellulose chain have three hydroxyl groups that give active binding sites to the dyes. For instance, in this case, FL is slightly soluble in hot ethanol while RB and MB are both soluble in alcohol at room temperature and have better access to the hydrogen bonding sites, and cellulose is known for being an effective sorbent of RB [60].

In this research, gel formation impregnation was not inspected purposely since the solubility of the model drugs in the alcohol can wash away most of the drug in the fiber production steps, namely regeneration and washing steps. Furthermore, a likely explanation for the inadequate drug loading efficiency of the post-treatment process as mentioned in Section 2.12 can be due to the low solubility of the compounds in the $scCO_2$ because of the presence of the polar groups in the drugs chemical structure. Therefore, solvent exchange loading is the best method for loading the aforementioned drug models or bioactive compounds with similar chemical structures. Using the solvent exchange process, both fabrication and loading of the aerogels can be conducted in one single preparation step.

Drug release data of the loaded CAF_{300} and CAF_{100} (Fig. 9A and B) exhibited an immediate release since most of the drug incorporated within the aerogel body was released in 300 min ($Q(\%) \geq 70\%$). When evaluating the drug release from aerogels, the specific surface area is one of the most important variables governing both the dissolution rate of the drug and its absorption in the aerogel body [61]. Other major factors are the diffusion path length and the solubility of the drug models in the release media as the chosen compounds have different solubility in water (in this study MB > RB ≫ FL) [62]. The CAF_{330} drug-loaded samples have a similar range of surface area and diffusion path length, the drug model water solubility will have a more significant role in the drug release. For instance, the slower release rate of the F_{330FL} arose from a more hydrophobic nature of FL and lowest water solubility in comparison to F_{330MB} and F_{330RB}. F_{330MB} higher drug released amount above 300 min can be also attributed to the highest solubility of MB in water. However, the CAF_{100} samples had a faster release rate in comparison to the CAF_{330} presumably due to the smaller diffusion path length and lower surface area and pore volume. The F_{100RB} had the highest surface area and pore volume between the CAF_{100} samples and displayed a slower release rate than the F_{100MB}. Nevertheless, the F_{100FL} exhibited the slowest release pace due to the significantly lower solubility of FL.

Therefore, the CAFs high specific surface area and the porous structure can lead to a rapid drug release for poorly water-soluble drugs such as FL. Such fast release of poorly water-soluble drugs has been investigated in other drug-eluting textiles such as nanofibers produced by the electrospinning technique [63,64]. This type of medical textiles with immediate drug release has been utilized for oral delivery or some circumstances where an instant reaction is required. For example, a fast release rate of antibiotics in the first hours following the biomaterial implantation is essential to prevent implant-related infection [20].

First-order kinetic model was not able to explain the drug release mechanism due to poor fitting of experimental data with the model and R^2 lower than 0.7 for all sample. Korsmeyer-Peppas could justify the release behavior better since R^2 was higher than 0.9 for all samples. The data of *m* and rate constant are shown in Table 5. The samples mainly exhibited Fickian diffusion, which occurs by the typical molecular diffusion of the drug due to a chemical potential gradient.

Modification of the cellulose aerogel fibers is necessary for tuning and extending the drug release since the storage and shipping of immediate drug-eluting textiles might be difficult. Furthermore, their inherent hydrophilicity and lack of cyclic wet stability can lower the long-term steadiness or limit the range of their application. Therefore, several chemical modifications, such as grafting with various hydrophobic groups and esterification, or physical treatments, such as plasma and polymeric coating, are possible strategies to achieve hydrophobized cellulose and overcome these issues.

Table 4
The experimental amount of loaded drug, drug loading efficiency (%), aerogel loading capacity (wt%), and specific loading (mg/m^2) of the solvent exchange impregnation process for the loaded CAFs.

Sample name	M_{exp} (mg)	Drug loading efficiency (%)	Aerogel loading capacity (wt%)	Specific loading (mg/m^2)
F_{330RB}	1.860 ± 0.069	36.4 ± 1.4	1.898 ± 0.071	13.5
F_{100RB}	1.666 ± 0.069	34.6 ± 1.4	1.701 ± 0.070	12.6
F_{330FL}	0.751 ± 0.0082	14.69 ± 0.16	0.7653 ± 0.0083	5.47
F_{100FL}	0.651 ± 0.0216	13.32 ± 0.42	0.663 ± 0.022	30.1
F_{330MB}	0.973 ± 0.057	17.8 ± 1.1	0.993 ± 0.059	6.32
F_{100MB}	0.84 ± 0.077	14.7 ± 1.5	0.857 ± 0.079	9.51

3.9. Cytotoxicity and cell viability analysis

The cell viability was observed in the CAFs after 1, 3 and 7 days of cell culture demonstrating that the fibrous meshes provided excellent conditions for cell viability and proliferation (Fig. 9C). The proliferation of fibroblast cells in the fibrous structure took place only from day 1 to day 3. This could be due to the fact that the cells reached a confluent layer after 3 days and thus there was no room for further proliferation of the cells. Moreover, 3D projection of the confocal microscopy images of the cells stained with live-dead staining with an imaging depth of 200 μm displayed no dead cells (in red) within the meshes after 7 days of culture (Fig. 9D).

The open porous structure of the CAFs allowed cell infiltration within the meshes. However, cell attachment was poor and therefore cells showed round morphology and did not proliferate inside the mesh. Fibroblast cells show elongated morphology both on adherent films and fibers [46,65]. For applications such as tissue engineering in which cell attachment is crucial, further physio-chemical surface modification is required. However, non-adherent meshes can be favorable products for some biomedical applications, such as wound dressing, to avoid damaging the newly formed tissue during the dressing removal [11,66].

4. Conclusion

In this study, wet spinning and $scCO_2$ drying were used to produce highly porous cellulose aerogel microfibers with large surface area (~100–180 m^2/g), high humidity absorption (~10–18 wt%), high water uptake capacity (3000–1000 wt%), low bulk density (~ 0.188 g/cm^3), and interconnected pores structures. The microfibers with different diameter were able to be transformed into knitted and needle punched textiles. Impregnation during the solvent exchange step was employed to load three model drugs. The drug-loaded fibers exhibited an immediate release while more than 70% of the loaded drugs were released within 300 min. The drug release mechanism was mainly Fickian based on the Korsmeyer-Peppas kinetic models. Cell studies demonstrated that

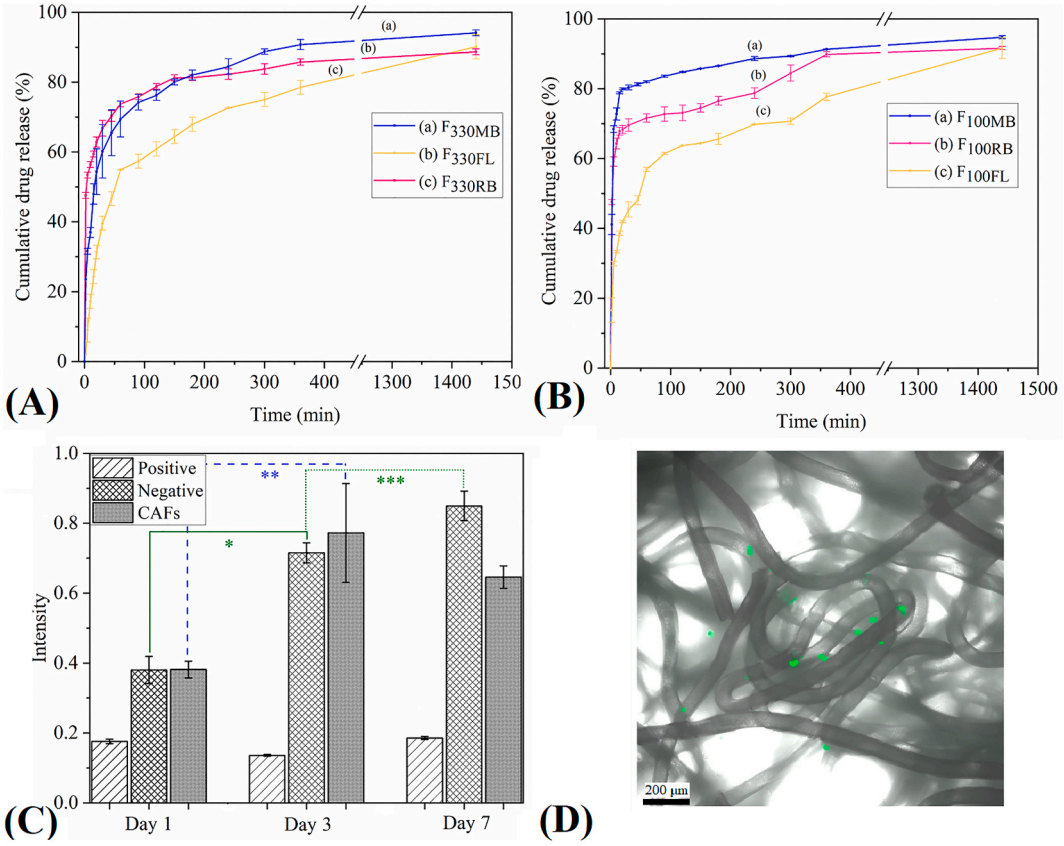

Fig. 9. Immediate drug release behavior of three model drugs of RB, FL, MB from (A) CAF300 and (B) CAF100. (C) XTT assay of the cellulose aerogel fibers; cell viability was observed in the samples in day 1, 3 and 7 of the experiment. Cell proliferation was detected from day 1 to day 3. The negative sample was polyethylene and the positive sample was a piece of a latex glove. (D) A representative confocal microscope image displaying live but poorly attached cells to the fibers (*$p < 0.05$).

Table 5
The power value of n and K_{kP} (constant of release rate) as parameters of Korsmeyer-Peppas for the drug-loaded fibers. The value of *m* determines the mechanism of release.

Sample name	m	R^2	Mechanism of release
F_{330RB}	0.12	0.98	Fickian
F_{100RB}	0.15	0.93	Fickian
F_{330FL}	0.84	0.93	non-Fickian
F_{100FL}	0.33	0.94	Fickian
F_{330MB}	0.35	0.98	Fickian
F_{100MB}	0.31	0.93	Fickian

the fibrous meshes have a great potential to be used for biomedical applications.

CRediT authorship contribution statement

Matin Rostamitabar: Conceptualization, Data curation, Formal analysis, Investigation, Methodology, Resources, Software, Validation, Visualization, Writing - original draft, Writing - review & editing. **Raman Subrahmanyam:** Conceptualization, Data curation, Formal analysis, Investigation, Methodology, Resources, Validation. **Pavel Gurikov:** Conceptualization, Investigation, Project administration, Supervision, Validation, Writing - review & editing. **Gunnar Seide:** Conceptualization, Investigation, Project administration, Supervision, Validation. **Stefan Jockenhoevel:** Conceptualization, Funding acquisition, Project administration. **Samaneh Ghazanfari:** Conceptualization, Data curation, Formal analysis, Funding acquisition, Investigation, Methodology, Project administration, Resources, Supervision, Validation, Writing - review & editing.

Declaration of competing interest

The authors declare that they have no known competing financial interests or personal relationships that could have appeared to influence the work reported in this paper.

Acknowledgements

The authors gratefully acknowledge the support of Hay Becker and Achim Besen (AMIBM, the Netherlands) in equipment upgrading and optimization as well as Arnold Wilbers from DSM (Geleen, the Netherlands) for his help in µ-CT assessments. We also thank Dr. Ulrich Moerschel from Textechno Herbert Stein GmbH & Co.KG (Moenchengladbach, Germany) for his support in mechanical analysis.

Funding

This project, as a part of the FibreNet consortium, has received funding from the European Union's Horizon 2020 - Research and Innovation Framework Programme under the H2020 Marie Skłodowska-Curie Actions grant agreement No. 764713.

Appendix A. Supplementary data

Supplementary data to this article can be found online at https://doi.org/10.1016/j.msec.2021.112196.

References

[1] T. Budtova, Cellulose 26 (2019) 81–121.
[2] L.-Y. Long, Y.-X. Weng, Y.-Z. Wang, Polymers 10 (2018) 623.

[3] V.T. Bartels, Handbook of Medical Textiles, Woodhead publishing, 2011.
[4] B.S. Gupta, 1 - manufacture, types and properties of biotextiles for medical applications, in: M.W. King, B.S. Gupta, R. Guidoin (Eds.) Biotextiles as Medical Implants, Woodhead Publishing, 2013, pp. 3–47.
[5] A. Corrias, M. Casula, M. Aegerter, M.K.N. Leventis, Aerogels Containing Metal, Alloy and Oxide Nanoparticles in Dielectric Matrices, Springer, New York, 2010.
[6] C.A. García-González, M. Alnaief, I. Smirnova, Carbohydr. Polym. 86 (2011) 1425–1438.
[7] H. Valo, S. Arola, P. Laaksonen, M. Torkkeli, L. Peltonen, M.B. Linder, R. Serimaa, S. Kuga, J. Hirvonen, T. Laaksonen, Eur. J. Pharm. Sci. 50 (2013) 69–77.
[8] J. Liu, F. Cheng, H. Grénman, S. Spoljaric, J. Seppälä, J.E. Eriksson, S. Willför, C. Xu, Carbohydr. Polym. 148 (2016) 259–271.
[9] H. Cai, S. Sharma, W. Liu, W. Mu, W. Liu, X. Zhang, Y. Deng, Biomacromolecules 15 (2014) 2540–2547.
[10] T. Hakkarainen, R. Koivuniemi, M. Kosonen, C. Escobedo-Lucea, A. Sanz-Garcia, J. Vuola, J. Valtonen, P. Tammela, A. Mäkitie, K. Luukko, M. Yliperttula, H. Kavola, J. Control. Release 244 (2016) 292–301.
[11] F.P. Soorbaghi, M. Isanejad, S. Salatin, M. Ghorbani, S. Jafari, H. Derakhshankhah, Biomed. Pharmacother. 111 (2019) 964–975.
[12] R. Subrahmanyam, P. Gurikov, I. Meissner, I. Smirnova, JoVE (113) (2016) 1–5, https://doi.org/10.3791/54116.
[13] M. Martins, A.A. Barros, S. Quraishi, P. Gurikov, S.P. Raman, I. Smirnova, A.R. C. Duarte, R.L. Reis, J. Supercrit. Fluids 106 (2015) 152–159.
[14] H. Jin, Y. Nishiyama, M. Wada, S. Kuga, Colloids Surf. A Physicochem. Eng. Asp. 240 (2004) 63–67.
[15] S. Hoepfner, L. Ratke, B. Milow, Cellulose 15 (2008) 121–129.
[16] S. Zhou, P. Liu, M. Wang, H. Zhao, J. Yang, F. Xu, ACS Sustain. Chem. Eng. 4 (2016) 6409–6416.
[17] R. Gavillon, T. Budtova, Biomacromolecules 9 (2008) 269–277.
[18] R. Sescousse, R. Gavillon, T. Budtova, J. Mater. Sci. 46 (2011) 759–765.
[19] S.M.K. Mohamed, K. Ganesan, B. Milow, L. Ratke, RSC Adv. 5 (2015) 90193–90201.
[20] M. Rostamitabar, A.M. Abdelgawad, S. Jockenhoevel, S. Ghazanfari, Macromol. Biosci., n/a (2021) 2100021.
[21] X. Lu, X. Shen, Carbohydr. Polym. 86 (2011) 239–244.
[22] S. Fischer, H. Leipner, K. Thümmler, E. Brendler, J. Peters, Cellulose 10 (2003) 227–236.
[23] M. Rostamitabar, G. Seide, S. Jockenhoevel, S. Ghazanfari, Appl. Sci., 11 (2021) 1525.
[24] S. Hoepfner, L. Ratke, Open Porous Cellulose Aerogel Fibers, 2008.
[25] I. Karadagli, B. Schulz, M. Schestakow, B. Milow, T. Gries, L. Ratke, J. Supercrit. Fluids 106 (2015) 105–114.
[26] J. Zhou, Y.-L. Hsieh, Nano Energy 68 (2020), 104305.
[27] B. Schulz, T. Meinert, D. Bierbüsse, M. Busen, N. Körtzinger, M. Stankowski, G. Seide, Chem. Ing. Tech. 88 (2016) 1501–1507.
[28] Z. Wang, H. Yang, Y. Li, X. Zheng, ACS Appl. Mater. Interfaces 12 (2020) 15726–15736.
[29] H. Yang, Z. Wang, Z. Liu, H. Cheng, C. Li, Polymers 11 (2019) 1899.
[30] Z. Liu, J. Lyu, D. Fang, X. Zhang, ACS Nano 13 (2019) 5703–5711.
[31] J. Li, J. Wang, W. Wang, X. Zhang, Molecules, 24 (2019) 1821.
[32] Y. Du, X. Zhang, J. Wang, Z. Liu, K. Zhang, X. Ji, Y. You, X. Zhang, ACS Nano 14 (2020) 11919–11928.
[33] G. Li, G. Hong, D. Dong, W. Song, X. Zhang, Adv. Mater. 30 (2018), 1801754.
[34] Z. Xu, Y. Zhang, P. Li, C. Gao, ACS Nano 6 (2012) 7103–7113.
[35] M.P. Batista, V.S.S. Gonçalves, F.B. Gaspar, I.D. Nogueira, A.A. Matias, P. Gurikov, Int. J. Biol. Macromol. 156 (2020) 773–782.
[36] S.-m Song, X.-l Hou, Y.-b Wu, S.-m Shuang, C. Yang, Y. Inoue, C. Dong, J. Lumin. 129 (2009) 169–175.
[37] D. Moreau, C. Lefort, R. Burke, P. Leveque, R.P. O'Connor, Biomed. Opt. Express 6 (2015) 4105–4117.
[38] R.E. Morsi, M. Elsawy, I. Manet, B. Ventura, Molecules 25 (2020) 3751.
[39] Y. Okuno, Y. Yamazaki, H. Fukutomi, S. Kuno, M. Yasutake, M. Sugiura, C.J. Kim, S. Kimura, H. Uji, ACS Omega 5 (2020) 772–780.
[40] L. Segal, J.J. Creely, A.E. Martin, C.M. Conrad, Text. Res. J. 29 (1959) 786–794.
[41] F. Fischer, A. Rigacci, R. Pirard, S. Berthon-Fabry, P. Achard, Polymer 47 (2006) 7636–7645.
[42] E. Haimer, M. Wendland, K. Schlufter, K. Frankenfeld, P. Miethe, A. Potthast, T. Rosenau, F. Liebner, Macromol. Symp. 294 (2010) 64–74.
[43] N.V. Mulye, S.J. Turco, Drug Dev. Ind. Pharm. 21 (1995) 943–953.
[44] 5 - mathematical models of drug release, in: M.L. Bruschi (Ed.) Strategies to Modify the Drug Release From Pharmaceutical Systems, Woodhead Publishing, 2015, pp. 63–86.
[45] R.W. Korsmeyer, R. Gurny, E. Doelker, P. Buri, N.A. Peppas, Int. J. Pharm. 15 (1983) 25–35.
[46] F. Kreimendahl, Y. Marquardt, C. Apel, M. Bartneck, G. Zwadlo-Klarwasser, J. Hepp, S. Jockenhoevel, J.M. Baron, J. Biomed. Mater. Res. A 107 (2019) 1340–1350.
[47] S. Ghazanfari, K.A. Alberti, Q. Xu, A. Khademhosseini, J. Biomed. Mater. Res. A 107 (2019) 1225–1234.
[48] M. Schestakow, I. Karadagli, L. Ratke, Carbohydr. Polym. 137 (2016) 642–649.
[49] M. Poletto, V. Pistor, A.J. Zattera, Cellulose-Fundamental Aspects vol. 2, 2013, pp. 45–68.
[50] J.-i Kadokawa, M.-a Murakami, A. Takegawa, Y. Kaneko, Carbohydr. Polym. 75 (2009) 180–183.
[51] X. Shang, H. Jiang, Q. Wang, P. Liu, F. Xie, Int. J. Mol. Sci. 20 (2019) 474.
[52] S. Park, J.O. Baker, M.E. Himmel, P.A. Parilla, D.K. Johnson, Biotechnol. Biofuels 3 (2010) 10.
[53] R.S. Dassanayake, S. Acharya, N. Abidi, Biopolymer-based materials from polysaccharides: properties, processing, characterization and sorption applications, in: Advanced Sorption Process Applications, IntechOpen, 2018.
[54] A. Abdulkhani, E. Hojati Marvast, A. Ashori, Y. Hamzeh, A.N. Karimi, Int. J. Biol. Macromol. 62 (2013) 379–386.
[55] R. Sescousse, R. Gavillon, T. Budtova, Carbohydr. Polym. 83 (2011) 1766–1774.
[56] G. Reichenauer, Structural characterization of aerogels, in: M.A. Aegerter, N. Leventis, M.M. Koebel (Eds.) Aerogels Handbook, Springer New York, New York, NY, 2011, pp. 449–498.
[57] Empirical Parameters of Solvent Polarity, Solvents and Solvent Effects in Organic Chemistry, 2010, pp. 425–508.
[58] M. Champeau, J.M. Thomassin, T. Tassaing, C. Jérôme, J. Control. Release 209 (2015) 248–259.
[59] Z. Ulker, C. Erkey, J. Supercrit. Fluids 120 (2017) 310–319.
[60] A. Kausar, R. Shahzad, S. Asim, S. BiBi, J. Iqbal, N. Muhammad, M. Sillanpaa, I. U. Din, J. Mol. Liq. 328 (2021), 115165.
[61] T.A. Esquivel-Castro, M.C. Ibarra-Alonso, J. Oliva, A. Martínez-Luévanos, Mater. Sci. Eng. C 96 (2019) 915–940.
[62] R.D. Lillie, H.J. Conn, HJ Conn's Biological Stains, Sigma Chemical Co, 1991.
[63] Y. Bai, D. Wang, Z. Zhang, J. Pan, Z. Cui, D.-G. Yu, S.-W. Annie Bligh, Polym. Test. 93 (2021), 106872.
[64] S. Kang, S. Hou, X. Chen, D.-G. Yu, L. Wang, X. Li, G.R. Williams, Polymers 12 (2020) 2421.
[65] S. Ghazanfari, S.M. Tafazoli, M.A. Shokrgozar, N. Haghighipour, N. Amirizadeh, R. E. Jafargholi, (2010).
[66] S. Saghazadeh, C. Rinoldi, M. Schot, S.S. Kashaf, F. Sharifi, E. Jalilian, K. Nuutila, G. Giatsidis, P. Mostafalu, H. Derakhshandeh, K. Yue, W. Swieszkowski, A. Memic, A. Tamayol, A. Khademhosseini, Adv. Drug Deliv. Rev. 127 (2018) 138–166.